

# Suzaku wide-band observations of SN 1006

Aya BAMBA<sup>1</sup>, Yasushi FUKAZAWA<sup>2</sup>, Junko S. HIRAGA<sup>3</sup>, John P. HUGHES<sup>4</sup>, Hideaki KATAGIRI<sup>2</sup>, Motohide KOKUBUN<sup>1</sup>, Katsuji KOYAMA<sup>5</sup>, Emi MIYATA<sup>6</sup>, Tsunefumi MIZUNO<sup>2</sup>, Koji MORI<sup>7</sup> Hiroshi NAKAJIMA<sup>6</sup> Masanobu OZAKI<sup>1</sup>, Rob PETRE<sup>8</sup>, Hiromitsu TAKAHASHI<sup>2</sup>, Tadayuki TAKAHASHI<sup>1</sup>, Takaaki TANAKA<sup>9</sup>, Yukikatsu TERADA<sup>3</sup>, Yasunobu UCHIYAMA<sup>1</sup>, Shin WATANABE<sup>1</sup>, Hiroya YAMAGUCHI<sup>5</sup>

<sup>1</sup>*Department of High Energy Astrophysics, Institute of Space and Astronautical Science (ISAS),  
Japan Aerospace Exploration Agency (JAXA),*

*3-1-1 Yoshinodai, Sagami-hara, Kanagawa 229-8510, Japan*

<sup>2</sup>*Department of Physics, Hiroshima University Higashi-Hiroshima, 739-8526, Japan*

<sup>3</sup>*RIKEN, cosmic radiation group, 2-1, Hirosawa, Wako-shi, Saitama, Japan*

<sup>4</sup>*Department of Physics and Astronomy, Rutgers University,  
136 Frelinghuysen Road, Piscataway, NJ 08854-8019, USA*

<sup>5</sup>*Department of Physics, Graduate School of Science, Kyoto University,  
Sakyo-ku, Kyoto 606-8502, Japan*

<sup>6</sup>*Department of Astrophysics, Faculty of Science, Osaka University, Toyonaka 560-0043, Japan*

<sup>7</sup>*Department of Applied Physics, Faculty of Engineering University of Miyazaki,  
1-1 Gakuen Kibana-dai Nishi, Miyazaki, 889-2192, Japan*

<sup>8</sup>*NASA Goddard Space Flight Center, Greenbelt, MD 20771, USA*

<sup>9</sup>*Stanford Linear Accelerator Center, 2575 Sand Hill Road M/S 29 Menlo Park, CA 94025 USA  
(AB): bamba@astro.isas.jaxa.jp*

(Received ; accepted )

## Abstract

We report on the wide band spectra of SN 1006 as observed by Suzaku. Thermal and nonthermal emission are successfully resolved thanks to the excellent spectral response of Suzaku's X-ray CCD XIS. The nonthermal emission cannot be reproduced by a simple power-law model but needs a roll-off at  $5.7 \times 10^{16}$  Hz = 0.23 keV. The roll-off frequency is significantly higher in the northeastern rim than in the southwestern rim. We also have placed the most stringent upper limit of the flux above 10 keV using the Hard X-ray Detector.

**Key words:** acceleration of particles — ISM: individual (SN 1006) — X-rays: ISM

## 1. Introduction

Since the discovery of cosmic rays nearly 100 years ago, their origin and acceleration mechanism has remained largely a mystery. The most widely accepted acceleration mechanism, at least for cosmic rays up to  $\sim 10^{15.5}$  eV (the knee energy), is diffusive shock acceleration at the rims of young supernova remnants (SNRs) (e.g., Bell 1978; Blandford & Ostriker 1978). This hypothesis has received indirect observation confirmation from the discovery using ASCA of synchrotron X-rays from the shell of the SN 1006, implying the presence of electrons accelerated to relativistic energy within the forward shocks of SNRs (Koyama et al. 1995). Recently, Bamba et al. (2003) suggested that the acceleration efficiency of electrons is quite high within the thin, filament-like shocks of SN 1006. This appears to be a common feature in young SNRs (e.g., Vink & Laming 2003, Yamazaki et al. 2004, Bamba et al. 2005, Ballet 2005, Vink 2006).

One key observational feature in the spectrum of synchrotron emission is a roll-off energy, which is determined by the maximum energy of accelerated electrons and the magnetic field. There are several measurements of the roll-off energy of the SN 1006 spectrum. Dyer et al. (2001) fit combined Rossi X-Ray Timing Explorer (RXTE) and ASCA spectra below 10 keV and measured a roll-off energy of  $3.0_{-0.2}^{+0.1} \times 10^{17}$  Hz. The spatial dependence of the roll-off energy is reported for the north-eastern rim (Bamba et al. 2003; Allen et al. 2004) and whole remnant (Rothenflug et al. 2004), but the conditions producing the variation is unclear. All these observations suffer from contamination by the low energy thermal emission. The 20–40 keV flux upper limit from the INTEGRAL ISGRI (Kalemci et al. 2006) implies that the roll-off is lower than 4 keV. To better measure the roll-off energy and its variation across the remnant, it is crucial to make X-ray observations with excellent statistics and energy response for diffuse emission, in order to subtract thermal emission parameters properly. The other need is the excellent sensitivity above 10 keV, in order to measure the synchrotron spectrum over as wide a band as possible. Suzaku (Mitsuda et al. 2007) is the best observatory for such studies. Suzaku has two sets of active instruments: four X-ray Imaging Spectrometers (XIS, Koyama et al. 2007) each at the focus of an X-Ray Telescope (XRTs, Serlemitsos et al. 2007) and a separate Hard X-ray Detector (HXD, Takahashi et al. 2007a; Kokubun et al. 2007). The XIS has two types of X-ray CCD, 3 front-illuminated (FI) CCDs and one back-illuminated (BI) one. The former have high quantum efficiency (QE) in the 2–12 keV band, whereas the BI CCD has high QE below 2 keV. The HXD’s silicon PIN diode array (hereafter PIN) has a narrow field of view (30 arcmin on a side) and an active background shield, as a result, is the most sensitive detector in the 10–70 keV band.

In this paper, we report the first results of wide-band Suzaku observations of SN 1006. §2 introduces the observations, our analysis and results is explained in §3, and we discuss our findings in §4. We assume the distance of SN 1006 to be 2.17 kpc (Winkler et al. 2003) in this paper.

## 2. Observations and Data Reduction

Suzaku observed SN 1006 and its background with 8 pointings, five for the SNR and three for the background, during the performance verification (PV) phase. We refer to each observation following the observation position, as shown in table 1. The data reduction and analysis were made using HEADAS software version 6.1.2., version 1.2 of the processed data, and XSPEC version 11.3.2.

The XIS was operated in the normal full-frame clocking mode without spaced-row charge injection in the all pointings. We filtered out data obtained during passages through the South Atlantic Anomaly (SAA), with elevation angle to the Earth’s limb below  $5^\circ$ , or with elevation angle to the bright Earth’s limb below  $13^\circ$ , in order to avoid the contamination of emission from the bright Earth. The XIS light curves in the NE observation show an increased background rate during 2006 September 9th 19:16–20:23. An X6.2 class solar flare was detected by the GOES satellite during 2006 September 9th, 19:13–20:36<sup>1</sup>. Thus, we ascribed the increased background rate to the solar flare and filtered out the flaring time. The net exposure times are listed in table 1.

The HXD PIN was operated in the normal mode. We filtered out the data obtained during passages through the South Atlantic Anomaly, with elevation angle to the Earth’s limb below  $5^\circ$ , and cut off rigidity (COR) smaller than 8 GV. The solar flare time in the NE observation is also filtered out. The net exposure in each observation is in table 1. The HXD team supplies two non-X-ray background (NXB) models, METHOD = PINUDLC (“bgd-a”) and METHOD = LCFIT (“bgd-d”) (Mizuno et al. Suzaku-Memo 2006-42, Watanabe et al. Suzaku-Memo 2007-01, Fukazawa et al. Suzaku-Memo 2007-02). In both models, METHODV=1.2 version is adopted. In this paper, we adopt the bgd-d model as we explain in §A1.

## 3. Analysis

### 3.1. XIS spectra

#### 3.1.1. Whole remnant

Figure 1 is the XIS 2.0–7.0 keV image, which shows the nonthermal rims on north-east (NE) and south-west (SW) regions.

We extracted combined spectra of the entire NE, SW1, and SW2 regions (see table 1), since the nonthermal rims are in these fields of view. The background spectrum was accumulated from the 3 background exposures (NE\_bg, SW\_bg1, SW\_bg2). We used 0.7–12.0 keV for the FI spectrum and 0.4–8.0 keV for the BI one. The 1.73–1.89 keV band is ignored, because the detector response function does not yet accurately model the Si edge. We also ignored the 5.7–6.6 keV band due to the contamination from internal calibration sources. Figure 2

---

<sup>1</sup> see <http://www.sec.noaa.gov/>

shows the background-subtracted spectra. In addition to strong emission lines below 2 keV, a hard component is clearly detected up to 12 keV. Therefore, we fitted the spectra using thermal plasma components plus a power-law continuum. The response files were constructed using `xisrmfgen` in the HEADAS package. The auxiliary response files were constructed using 0.5–10.0 keV XIS images and `xissimarfgen` (Ishisaki, et al. 2007) in the HEADAS software package. The thermal plasma model derived with Suzaku (Yamaguchi et al. 2007) is used, which has 3 non-equilibrium ionization components (two ostensibly for ejecta and one for heated interstellar medium (ISM)). For the absorption model, we used the cross sections of Morrison & McCammon (1983) and assumed solar abundances (Anders & Grevesse 1989). The absorption column was fixed at  $6.8 \times 10^{20} \text{ cm}^{-2}$  following the H I observation by Dubner et al. (2002). The XIS team reported the gain uncertainty of  $\sim \pm 5 \text{ eV}$  (c.f. Koyama et al. 2007), thus the gain is allowed to vary within a few percent separately for the FI and BI spectra.

The fit to this initial model is statistically unacceptable, with  $\chi^2/\text{d.o.f.}$  of 2513/589. The residuals show line-like structure in the low energy band, so we tuned the temperature and the ionization parameter of the heated interstellar medium components and the S abundance of high temperature ejecta, and fixed them again. We also adjusted the normalization factor between FI and BI spectra within a few percent. Serlemitsos et al. (2007) reported that the systematic error of the telescope vignetting is  $\sim 5\%$ , so the few percent adjustment of the relative normalization is reasonable. The best-fit models and parameters are shown in figure 2(left) and table 2. The reduced  $\chi^2$  improved to 2200/588, but is still statistically unacceptable. The residuals around the strong O lines are probably due to the calibration uncertainty in the low energy band (Koyama et al. 2007). The other large-scale residuals in the 2–10 keV band, on the other hand, cannot be due to calibration uncertainties. This result indicates that the nonthermal component cannot be represented by a simple power-law model.

We accordingly introduced the *srcut* model (Reynolds 1998) for the nonthermal component. The *srcut* model represents the synchrotron spectrum from an exponentially cut off power-law distribution of electrons in a homogeneous magnetic field. The radio spectral index is fixed to be  $\alpha = 0.57$  (Allen et al. 2001). The fit is still formally rejected (see the right panel of figure 2 and table 2), but the reduced  $\chi^2$  is substantially lower. (857/588). There are no large-scale residuals in the entire band.

### 3.1.2. NE and SW rims

We applied the thermal model plus the *srcut* continuum described above to the NE and SW rim spectra separately. The plasma parameters of the three thermal components were fixed at the values for the whole remnant (see table 2) except for the normalization. The best-fit models and parameters are shown in figure 3 and table 3, respectively. The fittings are statistically unacceptable again ( $\chi^2 = 553/338$  for NE and  $527/368$  for SW), but they show no large-scale structure.

### 3.2. HXD PIN spectra

SN 1006 is an extended source for the PIN as shown in figure 1. We therefore have to consider the effect of the PIN angular response for diffuse sources. In order to estimate the total efficiency for the entire SNR, we assumed that the emission region in the PIN energy band is the same as that of ASCA GIS 2–7 keV image available from Data Archives and Transmission System (DARTS<sup>2</sup>), which covers the entire remnant. The derived efficiency in each observation is shown in figure 4. The discontinuities around  $\sim 50$  keV are due to the Gd K-line back-scattered in GSO, and the enhancement above 50 keV in the SW\_bg1 effective area is due to the transparency of the passive shield which becomes larger in the higher energy band (Takahashi et al. 2007a). Takahashi et al. (2007b) checked the influence of the source size on the effective area for extended sources, and found that it has no energy dependence. The rim observations, NE, SW1, SW2, SE, and NW, have similar efficiency, while the background observations (NE\_bg, SW\_bg1, and SW\_bg2) have those of more than 1 order smaller. Thus, we combined 5 rim observations to improve statistics. The 3 background observations are also combined and used to evaluate the contribution of the cosmic X-ray background (CXB).

We first checked the background observations. Figure 5 (top-left) is the NXB-subtracted spectrum. Any residuals should be due to the cosmic X-ray background (CXB). We thus fit the 15–40 keV spectrum with a CXB model<sup>3</sup> by HEAO-1 (Boldt 1987) which has a photon index of 1.29 and a cut-off energy of 40 keV. We introduced a scaling factor to normalize the spectrum. The best-fit scaling factor value is  $1.39_{-0.22}^{+0.21}$  (errors indicate single parameter 90% confidence regions). The measured intensity fluctuations of the CXB flux are too small to account for this scaling factor value. ( $\sim 6\%$ ; Kushino et al. 2002). However, recent observations below 10 keV suggest a  $\sim 20\%$  higher CXB flux than that by Boldt (1987), as summarized in Frontera et al. (2006). Kokubun et al. (2007) reported that the PIN returns a  $\sim 13\text{--}15\%$  larger normalization than the XIS based on the most recent calibration using the Crab Nebula. Additionally, other papers using Suzaku data claim a similar normalization factor (1.15 for MCG  $-5\text{--}23\text{--}16$ ; Reeves 2007,  $1.10 \pm 0.05$  for MCG  $-6\text{--}30\text{--}15$ ; Miniutti et al. 2007). Serlemitsos et al. (2007) reported that the XIS normalization of the Crab Nebula agrees with previous satellite results (Toor & Seward 1974) within 3% error. The scaling factor should therefore be approximately  $1.2 \times 1.15 = 1.38$ , which is consistent with our best-fit value. We fixed the CXB component at the value by Boldt (1987) times 1.39, hereafter. Observations using Ginga indicate that excess emission local to SN 1006 (Lupus region) is restricted to soft X-ray band (Ozaki et al. 1994), consistent with our results.

Figure 5 (top-right) shows the NXB-subtracted spectrum from the rim observations. We applied the CXB component determined from the background observations (see the previous

---

<sup>2</sup> see <http://darts.isas.jaxa.jp/astro/> .

<sup>3</sup> see [http://heasarc.gsfc.nasa.gov/docs/suzaku/analysis/pin\\_cxb.html](http://heasarc.gsfc.nasa.gov/docs/suzaku/analysis/pin_cxb.html) .

paragraph). In the lower energy band, there seem to be some positive residuals in the 10–15 keV band, as shown in the bottom panel of figure 5, whereas we detected no signals from other energy bands. Note that systematic errors are not included in these figures. We added power-law component in order to estimate the residual flux. We fixed the photon index of the power-law component to be 3.0 and obtained a flux of  $2.7_{-1.0}^{+0.8} \times 10^{-5}$  ph cm<sup>-2</sup>s<sup>-1</sup>keV<sup>-1</sup> in 10–15 keV when no systematic errors are taken into account. We then checked the influence of systematic errors using the following process. Based on the HXD team report that the 90% systematic uncertainty of the background model in 15–40 keV is about 4% (figure 2 in appendix of Suzaku-Memo 2006-42), we constructed NXB spectra with 4% higher count rates. As before, we fit the NXB-subtracted spectrum with a CXB model. A significant signal is no longer detected in any energy band. The detection significance in the 10–15 keV band drops to  $1.2\sigma$ . The resulting 90% upper limits in several energy bands are listed in table 4. The best-fit flux for the 10–15 keV spectrum was  $2.7_{-1.0}^{+0.8}$  (statistics)  $\pm 3.6$  (systematic)  $\times 10^{-5}$  ph cm<sup>-2</sup>s<sup>-1</sup>keV<sup>-1</sup>.

### 3.3. Wide band spectra

Figure 6 shows the wide-band spectra in the 0.4–40.0 keV band. The CXB component for the PIN data described in §3.2 has already been subtracted. The solid and dotted lines represent the best-fit model (thermal + *srcut* model) in table 2. The normalization constant between XIS and PIN has been fixed at 1.15 (Kokubun et al. 2007). The nonthermal component is smoothly connected from the XIS band to the PIN band, although the systematic error of PIN prevented detection. A more quantitative evaluation of the spectrum above 10 keV might be possible with an improved NXB model of HXD PIN.

## 4. Discussion

We detected both thermal and nonthermal emission from the rims of SN 1006. The nonthermal component is described substantially better using an *srcut* model than a power-law model. The roll-off energy is  $5.69(5.67\text{--}5.71) \times 10^{16}$  Hz ( $\cong 0.23$  keV), the most precise measurement to date. This value is very close to that found for Tycho’s remnant ( $\sim 0.3$  keV; Cassam-Chenai et al. 2007). The upper limit on the flux above 10 keV with HXD PIN is more stringent than previous observations (Kalemci et al. 2006). The roll-off energy is slightly lower than previous results for the rim ( $2.6_{-0.7}^{+0.7} \times 10^{17}$  Hz; Bamba et al. 2003), and larger than those of inner regions ( $\sim 2 \times 10^{16}$  Hz; Rothenflug et al. 2004), but consistent with our use of an integrated spectrum of the SNR. Including high temperature components also would reduce roll-off energy. We treated the flux density at 1 GHz as a free parameter, and the result (16 Jy) is roughly consistent with the radio result ( $\sim 19$  Jy; Green 2006).

The *srcut* model have only three parameters, the flux and spectral index at 1 GHz, and the roll-off frequency. The former two parameters are well determined by radio observations.



The systematics are then governed only by the small uncertainties in these two parameters measured in the radio, and more significantly by the question of applicability of the model. The *srcut* model is a simple approximation of the emission from accelerated electrons. Recently, some papers report the acceleration is so efficient that the spectral shape deviates from the *srcut* model (e.g., Cassam-Chenai et al. 2007). More precise model for the emission from the accelerated electrons is needed. The fixed parameters in thermal plasma models also make systematic uncertainty.

The magnetic field strength can be estimated using the upper limit in the TeV band ( $3.5 \times 10^{-12}$  ergs cm<sup>-2</sup>s<sup>-1</sup> in the 0.26–10 TeV; Aharonian et al. 2005; Aharonian et al. 1997) under the synchrotron/inverse Compton scenario (in which the TeV photons are produced via the scattering of cosmic microwave background photons by the TeV electrons). The estimated lower limit of the magnetic field is  $\sim 25 \mu\text{G}$ , which is consistent with those estimated in other ways ( $40 \mu\text{G}$ ; Allen et al. 2001; Bamba et al. 2003).

The roll-off energy  $\nu_{roll}$  is described as

$$\nu_{roll} = 1.6 \times 10^{16} \left( \frac{B}{10 \mu\text{G}} \right) \left( \frac{E_e}{10 \text{ TeV}} \right)^2, \quad (1)$$

where  $E_e$  and  $B$  represent the maximum energy of accelerated electrons and the magnetic field strength respectively (Reynolds 1998; Reynolds & Keohane 1999). The maximum energy of electrons is estimated to be 9.4 TeV, under the assumption that the downstream magnetic field strength is  $40 \mu\text{G}$ , The time scale of synchrotron loss  $\tau_{loss}$  is

$$\tau_{loss} = 2.0 \times 10^4 \left( \frac{B}{10 \mu\text{G}} \right)^{-2} \left( \frac{E_e}{10 \text{ TeV}} \right)^{-1} \text{ [yrs]}, \quad (2)$$

then  $\sim 1300$  yrs in this case, roughly same as the SNR age. This result implies that the acceleration system in SN 1006 is changing from age-limited acceleration to synchrotron-loss limited acceleration.

The roll-off energy is significantly higher in the NE region, which is consistent with the XMM-Newton result (Rothenflug et al. 2004). This result implies that the magnetic field is stronger and/or electrons are accelerated to higher energy there. In other words, the acceleration efficiency is higher in the NE region. Assuming a magnetic field strength of  $40 \mu\text{G}$  again, we derived the maximum energy of electrons with eq.(1) to be 10 TeV (NE) and 8.5 TeV (SW), respectively.

## 5. Summary

We have presented wide band spectra of SN 1006 taking advantage of the excellent statistics and the low background of the Suzaku XIS and HXD. The nonthermal component has a roll-off energy of  $5.7 \times 10^{16}$  Hz. The HXD PIN provides the most stringent upper limit above 10 keV. The NE rim has the higher roll-off energy than the SW rim.

## Acknowledgements

We thank W. Hofmann for useful comments. We appreciate all members of the Suzaku team, with our particular thanks to the HXD hardware team members. The authors also thank K. Makishima, M. Ishida, and Y. Maeda for their fruitful comments. A. Bamba, H. Nakajima, H. Takahashi, T. Tanaka, and H. Yamaguchi are supported by JSPS Research Fellowship for Young Scientists.

## References

- Aharonian, F. A., Atoyan, A. M., & Kifune, T. 1997, *MNRAS*, 291, 162
- Aharonian, F., et al. 2005, *A&A*, 437, 135
- Allen, G. E., Petre, R., & Gotthelf, E. V. 2001, *ApJ*, 558, 739
- Allen, G. E., Houck, J. C., & Sturmer, S. J. 2004, *Advances in Space Research*, 33, 440
- Anders, E., & Grevesse, N. 1989, *Geochim. Cosmochim. Acta*, 53, 197
- Ballet, J. 2005, astro-ph/0503309
- Bamba, A., Yamazaki, R., Ueno, M., & Koyama, K. 2003, *ApJ*, 589, 827
- Bamba, A., Yamazaki, R., Yoshida, T., Terasawa, T., & Koyama, K. 2005, *ApJ*, 621, 793
- Bell, A. R. 1978, *MNRAS*, 182, 443
- Blandford, R. D., & Ostriker, J. P. 1978, *ApJ*, 221, L29
- Boldt, E. 1987, *Observational Cosmology*, 124, 611
- Cassam-Chenai, G., Hughes, J. P., Ballet, J., & Decourchelle, A. 2007, *ArXiv Astrophysics e-prints*, arXiv:astro-ph/0703239
- Dubner, G. M., Giacani, E. B., Goss, W. M., Green, A. J., & Nyman, L.-Å. 2002, *A&A*, 387, 1047
- Dyer, K. K., Reynolds, S. P., Borkowski, K. J., Allen, G. E., & Petre, R. 2001, *ApJ*, 551, 439
- Frontera, F., et al. 2006, *ArXiv Astrophysics e-prints*, arXiv:astro-ph/0611228
- Green D. A., 2006, ‘A Catalogue of Galactic Supernova Remnants (2006 April version)’, Astrophysics Group, Cavendish Laboratory, Cambridge, United Kingdom (available at ”<http://www.mrao.cam.ac.uk/surveys/snrs/>”).
- Ishisaki, Y. et al. 2007, *PASJ*, 59, S113
- Kalemci, E., Reynolds, S. P., Boggs, S. E., Lund, N., Chenevez, J., Renaud, M., & Rho, J. 2006, *ApJ*, 644, 274
- Kataoka, J. et al. 2007, *PASJ*, 59, 279
- Kokubun, M. et al. 2007, *PASJ*, 59, S53
- Koyama, K., Petre, R., Gotthelf, E.V., Hwang, U., Matsuura, M., Ozaki, M., & Holt S. S. 1995, *Nature*, 378, 255
- Koyama, K. et al. 2007, *PASJ*, 59, S23
- Kushino, A., Ishisaki, Y., Morita, U., Yamasaki, N. Y., Ishida, M., Ohashi, T., & Ueda, Y. 2002, *PASJ*, 54, 327
- Miniutti, G. et al. 2007, *PASJ*, 59, S315
- Mitsuda, K. et al. 2007, *PASJ*, 59, S1



- Morrison, R., & McCammon, D. 1983, *ApJ*, 270, 119
- Ozaki, M., Koyama, K., Ueno, S., & Yamauchi, S. 1994, *PASJ*, 46, 367
- Reeves, J. et al. 2007, *PASJ*, 59, S301
- Reynolds, S. P. 1998, *ApJ*, 493, 375
- Reynolds, S. P., & Keohane, J. W. 1999, *ApJ*, 525, 368
- Rothenflug, R., Ballet, J., Dubner, G., Giacani, E., Decourchelle, A., & Ferrando, P. 2004, *A&A*, 425, 121
- Serlemitsos, P. et al. 2007, *PASJ*, 59, S9
- Takahashi, T. et al. 2007a, *PASJ*, 59, S35
- Takahashi, T. et al. 2007b, *PASJ*, submitted
- Toor, A., & Seward, F. D. 1974, *AJ*, 79, 995
- Vink, J., & Laming, J. M. 2003, *ApJ*, 584, 758
- Vink, J. 2006, in *The X-ray Universe 2005*, ESA SP-604 Vol. 1,
- Winkler, P. F., Gupta, G., & Long, K. S. 2003, *ApJ*, 585, 324
- Yamaguchi, H., et al. 2007, *PASJ*, submitted
- Yamazaki, R., Yoshida, T., Terasawa, T., Bamba, A., & Koyama, K. 2004, *A&A*, 416, 595

## Appendix 1. Selection of HXD PIN background models

Two types of background models are provided by HXD team, bgd-a and bgd-d, and a comparison of these two models is useful for validating the background model for observations of interest. The NXB model of bgd-a was constructed by sorting earth occultation data using two parameters, PIN upper discriminator (PINUD) count rate and PINUD build-up counts. The former is used to take the COR dependence into account. The latter is a convolution of the PINUD counts with an exponential decay function with a certain time constant, and thus takes into account the activation-induced background component gradually decaying after the passage of South Atlantic Anomaly (Watanabe et al. Suzaku-Memo 2007-01). The NXB model of bgd-d was constructed so as to reproduce the light curve of the earth occultation data with an empirical model. The model parameters are such as PINUD, PINUD build up with 4 time constants, GSO high energy counts, and the angle between the HXD field of view and the magnetic field. The latter three parameters are used to model the activation-induced background variation. A set of monthly model parameters are determined by fitting the light curve of the Earth occultation data from each month (Fukazawa et al. Suzaku-Memo 2007-02). Basic features of reproducibility of both models are reported in Mizuno et al. (Suzaku-Memo 2006-42).

We found that, for observations of SN1006 in January 2006, bgd-a systematically gives  $\sim 7\%$  lower background flux than bgd-d (or vice versa). Although the reproducibility of the background model can be checked by looking at the earth occultation data in principle, observations of SN1006 unfortunately lacked the exposure to the earth. We therefore compared the 15–40 keV count rates of all the earth occultation data and background model prediction (both

bgd-a and bgd-d) with exposure more than 10 ks from 2005 September to 2006 March. Figure 7 shows the ratio between data and the NXB model prediction, which should be 1. We note that both bgd-a and bgd-d reproduce the data well within  $\sim 5\%$ , except for the period from the end of 2006 January to the beginning of 2006 February (5th month from 2005 September), where bgd-a gives a ratio larger than 1 by about 5%. In the figure, the period of SN1006 observations is indicated by red rectangles and 4 out of 8 observations are in the latter region. Since these 4 observations might have suffered from this anomaly, we adopted bgd-d as the NXB model in our analysis.

As the next step, we checked the background reproducibility in short periods by comparing the data count rate vs. data–bgd-d count rate for each 4096 sec interval in our 8 observations, which should be independent of the data count rate. The left panel of figure 8 shows the count rate vs. data – bgd-d in the 15–40 keV band. The data have a slightly positive correlation with the bgd-d model, but it is moderate. The right panel of figure 8 shows that the data–bgd-d have a small dispersion at the level of  $\sim 2 \times 10^{-2}$  count  $s^{-1}$ . This value is roughly similar to that of the CXB emission. Therefore, we concluded that the bgd-d model reproduces the real NXB in our observations and used it in this paper.

Note that the large residual found here is not generally seen and bgd-a and bgd-d provide us with consistent result most of the times, as shown by Reeves (2007), Miniutti et al. (2007), and Kataoka et al. (2007).

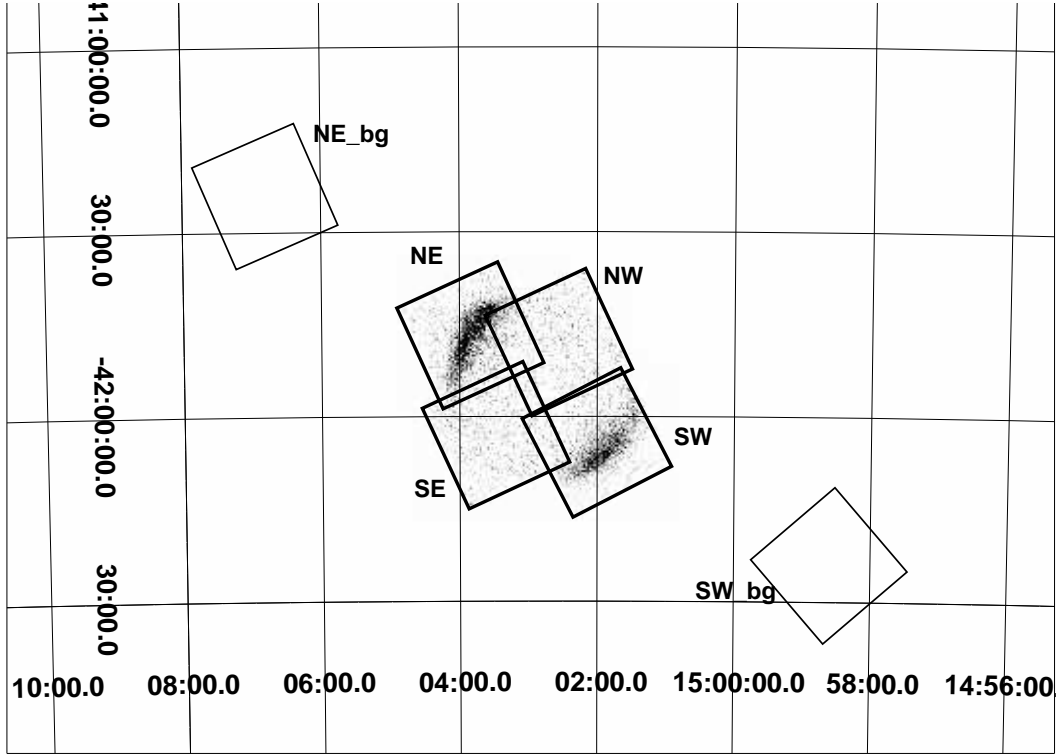


**Fig. 1.** XIS 2–7 keV image of SN 1006 (gray scale). Boxes represent XIS fields of view for the various pointings. Thick and thin box walls indicate rim and background observations, respectively. SW1 and SW2, and SW\_bg1 and SW\_bg2 have almost same field of view (see table 1), and thus are marked just as SW and SW\_bg in this figure.

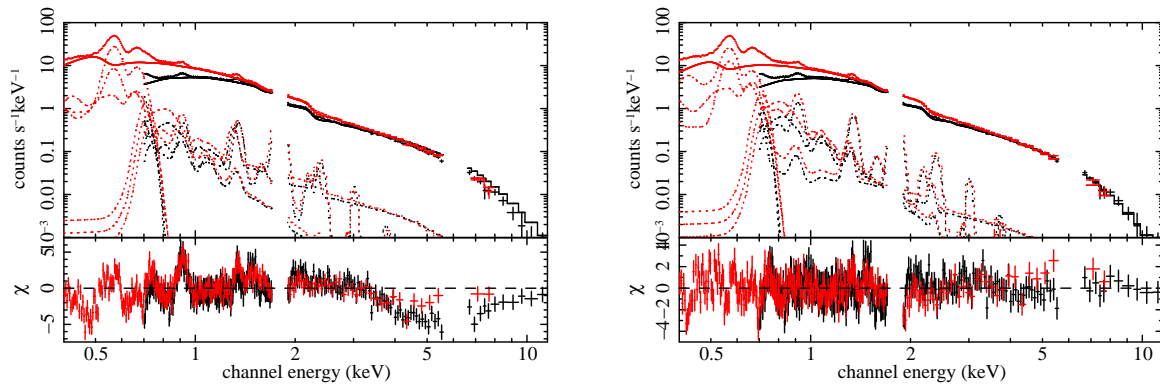


**Fig. 2.** XIS spectra with best-fit models of thermal + power-law (left) or thermal + *srcut* (right). Thermal and nonthermal models are represented with dotted or solid lines. Black and red represents FI and BI spectra, respectively. Lower panels in the figures are residuals from the best-fit models.

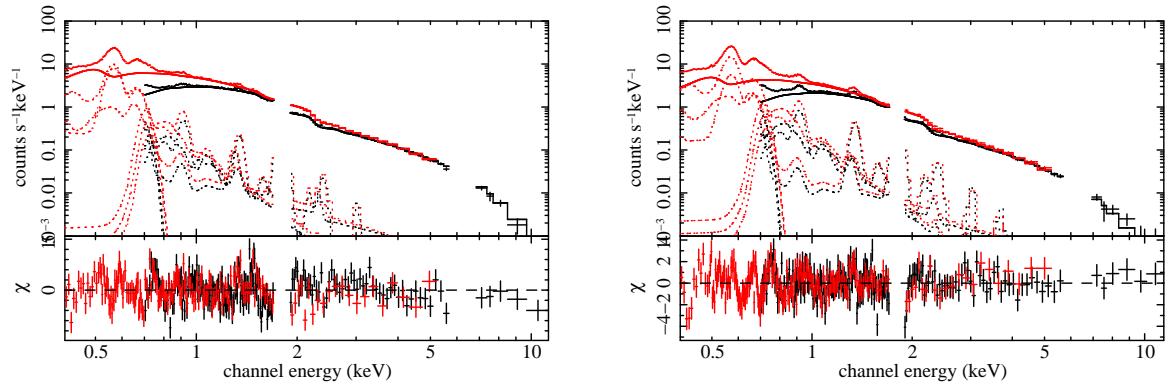


**Fig. 3.** XIS spectra of NE (left) and SW (right) regions. Thermal and nonthermal models are represented with dotted or solid lines. Black and red represents FI and BI spectra, respectively. Lower panels in the figures are residuals from the best-fit models.

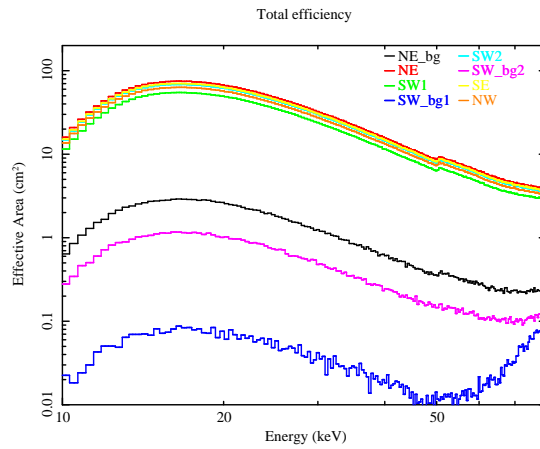


**Fig. 4.** The PIN effective area of each observation for the entire remnant.

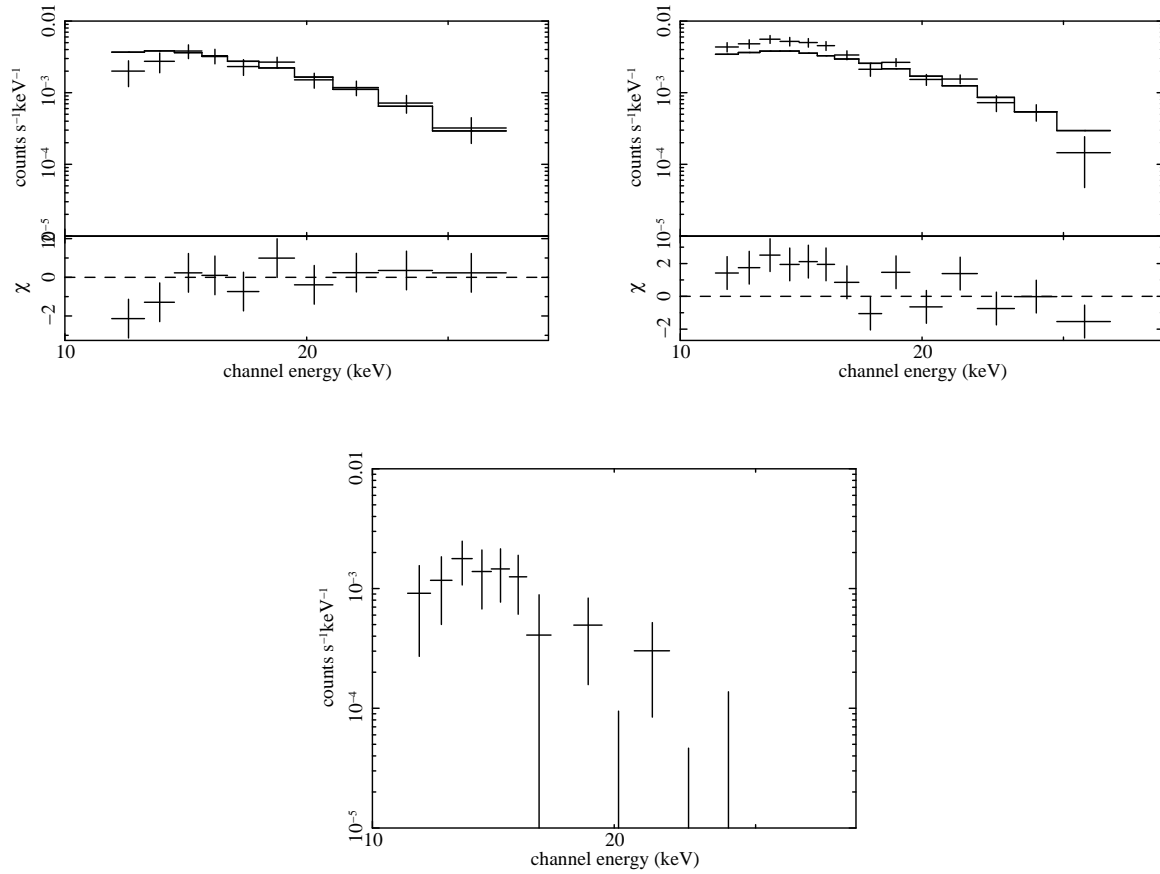


**Fig. 5.** Top: Background-subtracted PIN spectra for background (left) and rim (right) observations. Solid lines represent the best-fit CXB component. Bottom: Residuals of the rim data from the CXB component. Note that the systematic errors are not included.

**Table 1.** Observation Log.

	ObsID	Date	Aim point	Exposure (XIS/HXD)
		(yyyy/mm/dd)	(RA, Dec.)	(ks)
NE_bg.....	100019010	2005/09/04	(226.7005, -41.4006)	50/31
NE.....	100019020	2005/09/09	(225.9608, -41.7805)	43/31
SW1.....	100019030	2005/09/10	(225.5010, -42.0706)	31/22
SW_bg1.....	100019040	2005/09/11	(224.6505, -42.4005)	27/21
SW2.....	100019050	2006/01/26	(225.4998, -42.0701)	31/21
SW_bg2.....	100019060	2006/01/26	(224.6496, -42.4009)	30/25
SE.....	500016010	2006/01/30	(225.8686, -42.0508)	— <sup>a</sup> /48
NW.....	500017010	2006/01/31	(225.6397, -41.7993)	— <sup>a</sup> /51

<sup>a</sup>: Data is not used in our analysis.

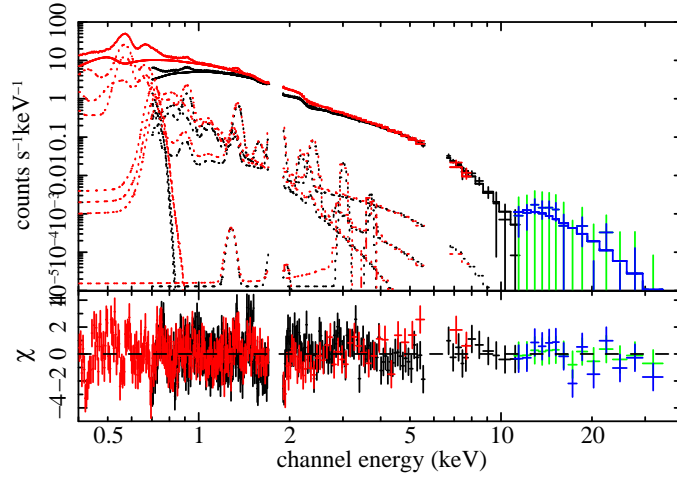


**Fig. 6.** Background-subtracted wide band spectra of XIS (black and red) and PIN (blue; without systematic errors, green; with systematic errors). The solid and dotted lines are the best-fit model for the XIS spectra (see table 2). The CXB component is also subtracted from the PIN data, thus the PIN data are basically same as the bottom panel of figure 5.

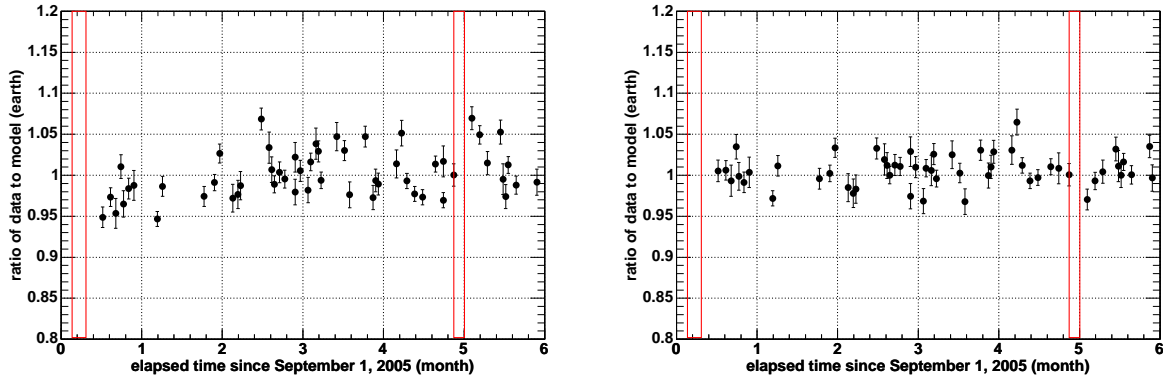


**Fig. 7.** The ratio between the 15–40 keV count rate of data and bgd-a (left) and bgd-d (right) during the earth occultation, from 2005 September to 2006 March. Red boxes represent the observation periods for SN 1006.



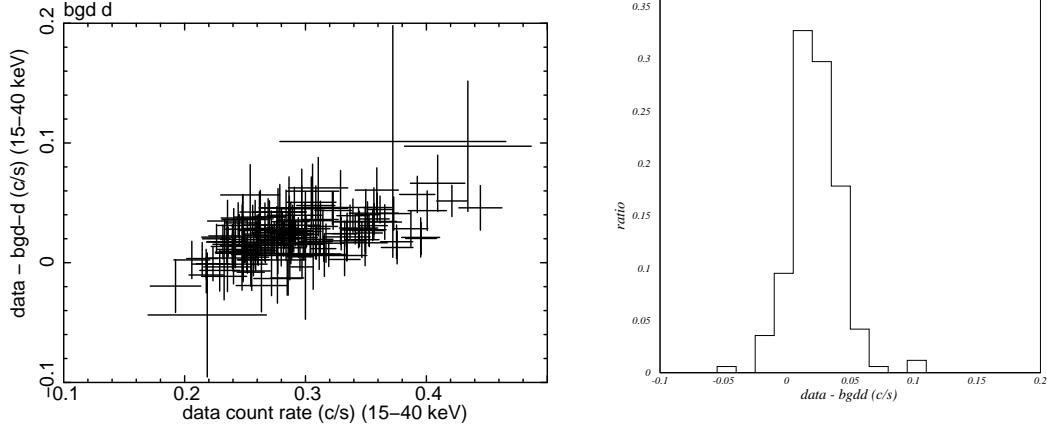


**Fig. 8.** (left) PIN data count rate vs. data–bgd-d model count rate. The energy band is 15–40 keV. (right) Histogram of data–bgd count rates with the bgd-d model.

**Table 2.** XIS spectral fitting parameters<sup>a</sup>.

Parameters	thermal <sup>b</sup> + power-law	thermal <sup>b</sup> + <i>srcut</i>
$N_{\text{H}}$ [cm <sup>-2</sup> ].....	6.8 × 10 <sup>20</sup> (fixed)	
VNEI 1 (ejecta 1)		
$kT$ [keV].....	1.2 (fixed <sup>b</sup> )	
$n_{\text{O}n_{\text{e}V}}$ [cm <sup>-3</sup> ].....	2.86 (2.45–3.06) × 10 <sup>52</sup>	4.19 (4.05–4.32) × 10 <sup>52</sup>
VNEI 2 (ejecta 2)		
$kT$ [keV].....	1.9 (fixed <sup>b</sup> )	
[S/O].....	2.7 (fixed)	
$n_{\text{O}n_{\text{e}V}}$ [cm <sup>-3</sup> ].....	8.43 (8.18–8.55) × 10 <sup>53</sup>	3.82 (3.77–3.89) × 10 <sup>53</sup>
NEI (ISM)		
$kT$ [keV].....	0.45 (fixed)	
$n_{\text{e}t}$ [cm <sup>-3</sup> s].....	5.7 × 10 <sup>9</sup> (fixed)	
$n_{\text{H}n_{\text{e}V}}$ [cm <sup>-3</sup> ].....	1.14 (1.06–1.21) × 10 <sup>56</sup>	3.45 (3.43–3.48) × 10 <sup>56</sup>
Nonthermal component		
$\Gamma/\nu_{\text{roll}}$ [—/Hz].....	2.73 (2.72–2.74)	5.69 (5.67–5.71) × 10 <sup>16</sup>
Norm [ph keV <sup>-1</sup> cm <sup>-2</sup> s <sup>-1</sup> at 1 keV/Jy at 1 GHz] ...	4.05 (4.04–4.07) × 10 <sup>-2</sup>	16.2 (16.1–16.3)
Gain offset for FI [eV].....	3.9	–1.4
Gain offset for BI [eV].....	–5.0	–4.0
$\chi^2/\text{d.o.f.}$ .....	2200/588	857/588

<sup>a</sup>: Parentheses indicate single parameter 90% confidence regions.

<sup>b</sup>: Thermal parameters are fixed following Yamaguchi et al. (2007).

**Table 3.** XIS spectral fitting parameters for NE and SW regions<sup>a</sup>.

Parameters	NE	SW
VNEI 1 (ejecta 1)		
$n_{\text{O}}n_{\text{e}}V$ [cm <sup>-3</sup> ] .....	1.20 (1.15–1.39) × 10 <sup>52</sup>	2.76 (2.61–2.83) × 10 <sup>52</sup>
VNEI 2 (ejecta 2)		
$n_{\text{O}}n_{\text{e}}V$ [cm <sup>-3</sup> ] .....	2.10 (2.06–2.15) × 10 <sup>53</sup>	1.88 (1.76–1.95) × 10 <sup>53</sup>
NEI 1 (ISM)		
$n_{\text{H}}n_{\text{e}}V$ [cm <sup>-3</sup> ] .....	1.09 (1.08–1.13) × 10 <sup>56</sup>	2.19 (2.16–2.24) × 10 <sup>56</sup>
<i>srcut</i>		
$\nu_{\text{roll}}$ [Hz] .....	6.66 (6.58–6.69) × 10 <sup>16</sup>	4.68 (4.64–4.73) × 10 <sup>16</sup>
Norm [Jy at 1 GHz] .....	7.72 (7.69–7.74)	8.33 (8.03–8.57)
Gain offset for FI [eV] .....	–2.0	–2.9
Gain offset for BI [eV] .....	–6.0	–4.0
$\chi^2/\text{d.o.f.}$ .....	553/338	527/368

<sup>a</sup>: Parentheses indicate single parameter 90% confidence regions.

**Table 4.** 90% upper-limits of nonthermal emission

Energy band	90% upper-limit [ph cm <sup>-2</sup> s <sup>-1</sup> keV <sup>-1</sup> ]
10 – 15 keV .....	7.1 × 10 <sup>-5</sup>
15 – 20 keV .....	2.3 × 10 <sup>-5</sup>
20 – 40 keV .....	8.8 × 10 <sup>-6</sup>